GEOPHYSICS, VOL. 78, NO. 2 (MARCH-APRIL 2013); P. S93–S103, 17 FIGS.
10.1190/GEO2012-0154.1

Imaging above an extended-reach horizontal well using converted shear waves and a rig source

Jakob B. U. Haldorsen[1], W. Scott Leaney[2], Richard T. Coates[2], Steen A. Petersen[3], Helge Ivar Rutledal[3], and Kjetil A. Festervoll[3]

ABSTRACT

We evaluated a method for using 3C vertical seismic profile data to image acoustic interfaces located between the surface source and a downhole receiver array. The approach was based on simple concepts adapted from whole-earth seismology, in which observed compressional and shear wavefields are traced back to a common origin. However, unlike whole-earth and passive seismology, in which physical sources are imaged, we used the observed compressional and shear wavefields to image secondary sources (scatterers) situated between the surface source and the downhole receiver array. The algorithm consisted of the following steps: first, estimating the receiver compressional wavefield; second, using polarization to estimating the shear wavefield; third, deconvolving the shear wavefield using estimates of the source wavelet obtained from the direct compressional wave; fourth, the compressional and shear wavefields were back projected into the volume between the source and receivers; where, finally, an imaging condition was applied. When applied to rig-source VSP data acquired in an extended-reach horizontal well, this process was demonstrated to give images of formation features in the overburden, consistent with surface-seismic images obtained from the same area.

INTRODUCTION

Borehole-seismic data generated with an acoustic source on the surface and an array of multicomponent receivers in a wellbore are typically used to image structures below the receiver tool. The wavefield recorded at the receiver array is separated into downgoing and upgoing wavefield components (and sometimes into compressional and shear), and the upgoing are deconvolved with an effective source signature estimated from the downgoing components (see, e.g., Haldorsen et al., 1994). The deconvolved compressional or shear waves can be used to create images of the formation below the well using a variety of migration algorithms designed for this purpose (e.g., Miller et al. [1987] as Haldorsen [2002] applies).

Using converted shear waves

Bostock et al. (2001) and Shragge et al. (2001) report a method to decompose the arrivals from teleseismic (distant) events recorded on a surface receiver array into compressional and shear waves components. Rondenay et al. (2001) apply this to generate an image of the so-called Moho discontinuity — the boundary between the earth crust and mantle — located about 40 km below a surface array of receivers. Similar methods have been used for finding the locations of epicenters in earthquakes and in passive seismic monitoring (e.g., Michaud et al., 2004).

Rondenay et al. (2001) image the Moho using a primary compressional signal, originating from some far-away earthquake and incident on the Moho from below. The compressional signal is partially converted to shear at the Moho, and the two modes are subsequently recorded by an array of 3C surface receivers. The Moho is imaged as a distribution of sources of the secondary shear mode. Chen et al. (2010) use the same technique but compare different ways of deconvolving the shear by the compressional to ascertain that the measured shear and compressional signals have the same origin.

In either of these methods, the distance to the microseismic or earthquake hypocenter (Michaud et al., 2004) or to the shear conversion point (Rondenay et al., 2001; Chen et al., 2010) is determined from the time delay between compressional and shear waves.

We assume that the source primarily generates a compressional signal. (Equivalently, we restrict our consideration to the time window after the first arrival that precedes the direct shear wave arrival.) Along the path from the source to the receivers, the

Manuscript received by the Editor 29 April 2012; revised manuscript received 16 August 2012; published online 4 February 2013.
[1]Formerly Schlumberger WesternGeco, Houston, Texas, U.S.A.; presently READ ASA, Hvalstad, Norway. E-mail: jakobhaldorsen@gmail.com.
[2]Schlumberger WesternGeco, Houston, Texas, U.S.A. E-mail: leaney@houston.oilfield.slb.com; rtcoates@slb.com.
[3]Statoil ASA, Sandsli, Norway. E-mail: steap@statoil.com; HERUT@statoil.com; kafe@statoil.com.

downgoing compressional wave encounters acoustic impedance heterogeneities that reflect, refract, and distort it. In addition, some of the direct compressional wave may be converted to shear waves. If we assume the converted shear wave travels alongside the compressional wave, then the delay Δt^{ps} at the receiver is determined by the difference in propagation slowness (inverse velocity) for these two types of waves. Denoting the compressional propagation velocity by V_P, the shear velocity by V_S, the distance d from the conversion point to the receiver can in its simplest form be found from

$$d = \frac{\Delta t^{ps}}{\frac{1}{V_S} - \frac{1}{V_P}}. \quad (1)$$

If we assume that the compressional and shear emanating from a conversion point are orthogonal, the direction of the back projection to the conversion point could be either along the polarization of the compressional or in the direction orthogonal to the polarization of the secondary, converted shear component of the wavefield (e.g., Rondenay et al., 2001; Michaud et al., 2004).

In this paper, we apply concepts similar to these to vertical seismic profile (VSP) data recorded by a downhole array using a surface source that is laterally offset from the receivers. The objective of the method is to generate images of structures located between the source and the receivers, which convert a part of the compressional energy to shear.

CONVERTED-WAVE IMAGING

Figure 1 illustrates how the shear-conversion technique can apply to VSP data when the conversion takes place along a planar interface. The figure shows an extended-reach well with a rig source and a downhole receiver array. The horizontal interface between the two shades of gray illustrates an acoustic contrast. In the figure, the incident downgoing compressional wave (the propagation direction indicated by the red dotted arrow) is split at this contrast into a refracted downgoing compressional ray (blue dotted arrow) and a downgoing shear wave polarized in the vertical plane (yellow dotted arrow). Data recorded by a VSP tool inside the medium, in the presence of an acoustic interface, will include the refracted or scattered compressional wavefield in addition to the converted shear.

However, whereas equation 1 is valid for a "point conversion" if the wavefield conversion takes place along a planar interface, the range of "scattering angles" observed by the VSP receiver array may be quite limited and render a point conversion approach to the imaging less useful. For wavefield conversions along a (at least piecewise) planar interface, the propagation direction of the different wavefield components is governed by Snell's law from elementary ray theory. The propagation direction is determined by the orientation of the interface as well as the propagation velocities of one wavefield relative to the other, and the two wavefield components, originating at the same location, will reach the wellbore at different receivers and have traveled a different distance.

Figure 2 illustrates Snell's law for a planar, dipping interface, including the three wavefields in play for this problem: the compressional incident on the converting interface, the refracted compressional, and the converted, refracted shear. Let us first assume that the interface is parallel with the array ($\alpha \approx 0$ in Figure 2). In this case, the time delay is determined by the difference in the components of the slowness vector perpendicular to the interface (and the array), independent on the angle of incidence on the conversion plane of the source compressional field (θ'_p in Figure 2). With θ_p and θ_s denoting the angles of incidence on the array of the two wavefield components, we have the distance a between the conversion plane and the receiver array given by (for the parallel plane and array)

$$a \approx \frac{\Delta t^{ps}}{\frac{\cos\theta_s}{V_S} - \frac{\cos\theta_p}{V_P}}. \quad (2)$$

This is a modified version of equation 1 for the distance to the conversion point back along the ray of the refracted compressional wavefield incoming on the array

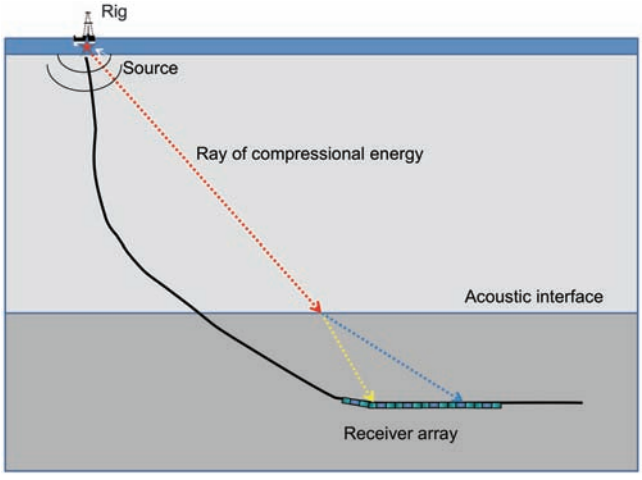

Figure 1. An extended-reach well with a rig source and a downhole receiver array. The shades of gray illustrate different formations with different acoustoelastic properties. The incident downgoing compressional wave (the propagation direction indicated by the red dotted arrow) is split at the interface between the two materials into a refracted downgoing compressional ray (blue dotted arrow) and a downgoing shear wave, polarized in the vertical plane (yellow dotted arrow).

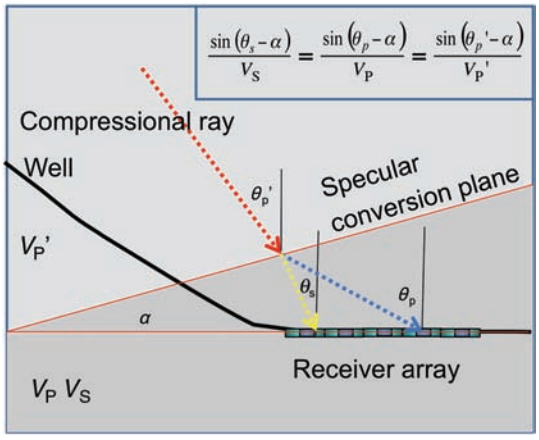

Figure 2. Illustration of Snell's law, relating the relative angle α between the conversion interface and receiver array to the angles of incidence on the array of the transmitted refracted compressional (blue dotted arrow) and a downgoing shear wave, polarized in the vertical plane (yellow dotted arrow). The shades of gray illustrate different formations with different acoustoelastic properties. The incident downgoing compressional wave (the propagation direction indicated by the red dotted arrow).

$$d_p \approx \frac{\Delta t^{ps}}{\frac{\cos\theta_s}{\cos\theta_p}\frac{1}{V_S} - \frac{1}{V_P}}. \quad (3)$$

Next, we consider the array rotated by an angle α to give the geometry shown in Figure 2. With the angles θ denoting the angles of incidence on the receiver array, we have to replace the θs in equation 3 by $\theta - \alpha$. With this substitution, we have the local distances back to the "specular conversion" plane

$$d_p \approx \frac{\Delta t^{ps}}{\frac{\cos(\theta_s-\alpha)}{\cos(\theta_p-\alpha)}\frac{1}{V_S} - \frac{1}{V_P}}. \quad (4)$$

Snell's law allows the ray angle θ_s for the shear wavefield to be replaced

$$d_p \approx \frac{\Delta t^{ps}}{\frac{\sqrt{1-\left(\frac{v_S}{v_P}\right)^2\sin^2(\theta_p-\alpha)}}{\cos(\theta_p-\alpha)}\frac{1}{V_S} - \frac{1}{V_P}}. \quad (5)$$

Depending on what is most convenient, one may want to use either of equation 4 or 5 for the back-propagation to the conversion point. If one can make separate measurements of θ_s and θ_p, Snell's law will provide a constraint on the dip angle α. For cases in which the separation of the compressional and converted shear incoming on the array is not well resolved, one may use equation 5 with assumed formation dips.

In any of the equations 1 through 5, and depending on the level of information available, the compressional and shear slownesses can be regarded as the "effective slowness," averaged along the raypaths between the conversion point and the receiver array. In our application, we calculate the traveltimes using an eikonal ray tracer, like that described by, e.g., Cao and Greenhalgh (1994) and Sethian (1996). Using equation 5 for extrapolating along the compressional wave, the local shear velocity model is modified by the trigonometric term appearing in the denominator, accounting for the difference in travel path of the recorded compressional and converted shear. We also assume that the conversion interface is approximately parallel to the receiver array ($\alpha \approx 0$ in equation 5).

Migration

In the conventional approach to migrating converted waves, one assumes that all converted shear waves are generated from the downgoing compressional wave via a single scattering mechanism at a distribution of point scatterers. This requires modeling the forward propagating compressional field from the source through the overburden and modeling the backward propagation of the shear wavefield from the receivers. An imaging condition — that wherever the two wavefield coexist corresponds to a scatterer — is imposed to generate the migrated image. The strength of each scatterer is given by the deconvolution of the extrapolated recorded field with the extrapolated source field (this deconvolution is equivalent to a weighted or normalized correlation between the two wavefields). This approach requires a complete compressional and shear velocity model through which to model the propagation. This may be problematic particularly in complex structural regions.

In contrast, using the method described in the preceding sections, we see that close to the wellbore, we may generate the image by extrapolating the wavefield back in time along the shear and compressional rays, and the location of the conversion point is wherever the back-propagated compressional and shear waves coexist. This has the advantage of requiring only compressional and shear velocity models local to the well.

The polarization of the converted shear at the location of the receiver is found either from a prior explicit wavefield separation (e.g., according to Leaney and Esmersoy, 1989) or, alternatively, from geometric considerations. A given particle motion, as measured by the VSP tool at the borehole wall, could be caused by a compressional wave in the direction of this motion, or by a shear wave perpendicular to this. In assuming that the compressional field is polarized along the ray connecting the scattering/conversion point to the receiver location and that the polarization of the shear is perpendicular to this ray, Haldorsen (2002) shows that vector-based migration using traveltimes in combination with polarization is sufficient for separating compressional and shear contributions to an image. His assumptions allow the wavefield separation to be done inside the migration kernel by projecting the recorded wavefields onto and perpendicular to the connecting rays (in general, the shear and compressional rays are different). With the direction of the ray described by its azimuthal angle φ and polar angle θ, the separation in 3D space of the three principal components for a wavefield propagating in a 2.5D medium can be achieved by two successive rotations

$$\begin{pmatrix} u_p \\ u_{sh} \\ u_{sv} \end{pmatrix} = \begin{pmatrix} \cos\theta & 0 & \sin\theta \\ 0 & 1 & 0 \\ -\sin\theta & 0 & \cos\theta \end{pmatrix} \times \begin{pmatrix} \cos\varphi & \sin\varphi & 0 \\ -\sin\varphi & \cos\varphi & 0 \\ 0 & 0 & 1 \end{pmatrix} \begin{pmatrix} u_x \\ u_y \\ u_z \end{pmatrix}, \quad (6)$$

where u_x, u_y, and u_z are the inline, transverse, and vertical components and u_p, u_{sh}, and u_{sv} are the compressional, the shear polarized in the transverse, horizontal direction, and shear polarized in the vertical plane, respectively. For a medium with a general 3D velocity gradient, the relationship in equation 6 between the measured (horizontal, vertical) components and the (compressional, shear) components will not be valid far away from the receiver array. For our quasi-2D geometry generating images close to the receiver array, we will assume that equation 6 is valid and also that we can ignore the horizontal shear, setting the azimuthal angle φ to 0.

For each 2C receiver (the inline horizontal component and the vertical component), we calculate the traveltimes to a point in the (2D) image space by short-distance ray tracing through a given 2D velocity model. The corresponding vector trace is projected onto the ray for the compressional refracted/scattered component and perpendicular to the ray for the converted-shear component, according to equation 6. The two wavefields "back projected" from the receiver location $\mathbf{r}$ to the image point $\mathbf{x}$ can be written as

$$\begin{aligned} |u_p^{\mathbf{r}}(\omega)|e^{i\omega(t-t^p_{\mathbf{rx}})} &= |u_x^{\mathbf{r}}(\omega)\cos\theta_{\mathbf{rx}} + u_z^{\mathbf{r}}(\omega)\sin\theta_{\mathbf{rx}}|\, e^{i\omega(t-t^p_{\mathbf{rx}})} \\ |u_{sv}^{\mathbf{r}}(\omega)|e^{i\omega(t-t^s_{\mathbf{rx}})} &= |-u_x^{\mathbf{r}}(\omega)\sin\theta_{\mathbf{rx}} + u_z^{\mathbf{r}}(\omega)\cos\theta_{\mathbf{rx}}|\, e^{i\omega(t-t^s_{\mathbf{rx}})}. \end{aligned} \quad (7)$$

With only one point refractor giving a single polarized impulse motion vector recorded on receiver n, we will get a cosine-tapered and a sine-tapered projection of this impulse vector on to the two orthogonal components u_p and u_{sv}. A point refractor will give transmitted wavefields with distinct radiation patterns for compressional and converted shear. With a wide enough acquisition aperture, it is commonly assumed that the migration operation will sort these radiation patterns out as images are formed by stationary-phase sums along coherent wavefronts.

The imaging condition is that the two transmitted wavefields, the compressional and the converted shear, coexist at location $\mathbf{x}$, a condition that could be measured by correlating the back-propagated converted shear with the back-propagated compressional fields. A more appropriate measure would be deconvolution of the converted shear by the transmitted compressional (with $u_p(\omega) = 1$, correlation and deconvolution are the same). Deconvolving the back-propagated shear with the back-propagated compressional wavefields gives

$$\begin{aligned} C^{\mathbf{rx}}_{p,sv}(\omega) &= |u^{\mathbf{r}}_{sv}(\omega)| A^{\mathbf{rx}}_{sv}\, e^{i\omega(t-t^{s}_{\mathbf{rx}})} \quad |u^{\mathbf{r}}_{p}(\omega)|^{-1} A^{\mathbf{rx}-1}_{p} e^{-i\omega(t-t^{p}_{\mathbf{rx}})} \\ &= |u^{\mathbf{r}}_{sv}(\omega)|\, A^{\mathbf{rx}}_{sv} e^{i\omega\,(t-(t^{s}_{\mathbf{rx}}-t^{p}_{\mathbf{rx}}))} \quad |u^{\mathbf{r}}_{p}(\omega)|^{-1} A^{\mathbf{rx}-1}_{p}\, e^{-i\omega t} \\ &\approx |u^{\mathbf{r}}_{sv}(\omega)||u^{\mathbf{r}}_{p}(\omega)|^{-1}\, e^{-i\omega\,(t^{s}_{\mathbf{rx}}-t^{p}_{\mathbf{rx}})}. \end{aligned} \tag{8}$$

This is the same result as if we would project the deconvolved converted shear a distance back into the formation given by equation 5: the difference in measured arrival time divided by the difference in slowness. Here, $A^{\mathbf{rx}}$ is a geometric spreading term extrapolating from point $\mathbf{r}$ to point $\mathbf{x}$. It is assumed that the spreading term for the S_V and the P-waves are approximately the same.

The conversion-point image is obtained by applying an inverse Fourier transform and summing over the receivers

$$I(\mathbf{x}) = \sum_r \int d\omega C^{\mathbf{rx}}_{p,sv}(\omega) e^{-i\omega t}. \tag{9}$$

With data deconvolved by the estimated direct compressional wavefield component, one would only need to consider the S_V components. When the converted shear can be paired with the direct compressional (with geometries like those in Figures 1 and 2), the transversely projected values of the data should be taken at times $t = t^{p}_{\mathbf{sr}} + \Delta t^{ps}_{\mathbf{rx}} = t^{p}_{\mathbf{sr}} + t^{s}_{\mathbf{rx}} - t^{p}_{\mathbf{rx}}$, where $t^{p}_{\mathbf{sr}}$ is the arrival time of the direct compressional component of the wavefield. Here, $t^{p}_{\mathbf{sr}}$ is obtained from picking traveltimes on the recorded data and $t^{s}_{\mathbf{rx}}$ and $t^{p}_{\mathbf{rx}}$ are obtained from short-range ray tracing through a given velocity model from the receiver location $\mathbf{r}$ to the image point at $\mathbf{x}$. If the recorded data traces have been deconvolved using the complete estimated direct compressional wavefield, the direct traveltimes $t^{p}_{\mathbf{sr}}$ have been removed and we should use the projected values of the deconvolved wavefield at $\Delta t^{ps}_{\mathbf{rx}}$. One could look at this as pegging the image on the well trajectory.

For a horizontal interface, the converted shear will be polarized in the vertical plane. If the interface is perpendicular to the ray, no shear energy will be converted. The rate of conversion will be particularly high for an incident compressional wave grazing the interface; i.e., the preferred geometry for this technique will have a source that is displaced horizontally from the receiver array.

In the section "Comparison to other related methods," we discuss the distinction between the method presented here and salt-proximity surveys and interferometry methods.

Deconvolution

The converted shear event will be coherent with the primary compressional event; meaning that however complicated the primary compressional signal is, the secondary converted shear will have the same complexity. Deconvolving the total recorded wavefield with an estimate of the complicated incoming compressional wave will therefore compress the converted shear signal and make it suitable for imaging. This is what is conventionally done in the processing of VSP data.

For the deconvolution, we use the "semblance-weighted" deconvolution operator described by Haldorsen et al. (1994), designed to broaden the spectrum of the estimated source signal at the same time as minimizing any additional signal present in the data:

$$F_n(\omega) = \frac{f^*_n(\omega)}{E_n(\omega)} = \frac{f^*_n(\omega)}{|f^*_n(\omega)|^2} \frac{|f^*_n(\omega)|^2}{E_n(\omega)}, \tag{10}$$

where $f_n(\omega)$ is a frequency-domain estimate of the source signal at depth level n, $E_n(\omega)$ is an estimate of the total energy at the same depth level, and ω is the angular frequency. This filter will compress the downgoing compressional field and any signal that is coherent with this, including the converted downgoing field.

Process summary

Preprocessing the VSP data prior to imaging is very much like a standard processing of borehole-seismic data. Processing includes the following essential steps:

1) Average data traces recorded at coincident source and receiver locations.
2) Orient the 3C data traces into a polarization of particle movement along a vertical axis and two horizontal axes, one in the plane of the well and one in a direction perpendicular to the well.
3) Pick traveltimes for the compressional wave traveling directly from the source to the receivers (find the "break times" t_n).
4) Estimate the waveform of the direct compressional signal maximizing the amplitude within a short window around the time of these break times.
5) Deconvolve all x-, y-, and z-components of the wavefield by the estimated "downgoing" compressional field using the semblance-weighted operator described by equation 10.
6) For given velocity models, calculate the traveltimes for a compressional (t^p_n) and shear polarized in the vertical plane (t^s_n) from each (x, y)-point in the image space to all receivers.
7) Find the difference $\Delta t^{ps}_n = t^s_n - t^p_n$ between the compressional and shear traveltimes.
8) Using the deconvolved total wavefield, find the vector of particle motion at the receivers at times $t_n + \Delta t^{ps}_n$
9) For each receiver, find the component of the vector of particle motion perpendicular to the ray connecting the receiver and the image point ("projection" step).
10) For each point in image space, sum the projected contributions for all receivers using appropriate weights from standard migration theory (we have used the weights that Miller et al. [1987] describe).

For the estimation of traveltimes, we use velocity models provided from the outside, adjusted locally using the direct arrivals

at the receivers. The compressional velocity model is adjusted so that the computed traveltimes t_n^p at receiver n exactly agree with the picked traveltimes t_n. Because the distance to the estimated shear conversion point is essentially determined by the difference between the model shear and compressional slownesses (equation 1), it may be expected that, even more so that related processes based on migration (or wave equation), our approach is susceptible to errors in the velocity models. The more accurate these models are, the better the results. However, as the extrapolation from the receivers into the formation is local, using local velocities (or slownesses), the models may straightforwardly be calibrated using the shear and compressional waves observed locally at the receiver array.

Comparison to other related methods

Salt-proximity surveys have been used in the industry since the 1930s. The conventional salt-proximity approach uses estimates of the compressional velocities in the salt and surrounding sediments together with the compressional arrival time, and sometimes polarization, to estimate the location of the surface of the salt body at which the ray joining source to receiver exits the salt.

Recent work by Zhao et al. (2006) extends the conventional approach to use the arrival time of the compressional-to-shear conversion together with the compressional velocity in the salt and shear velocity in the sediments, respectively. However, neither the conventional approach nor Zhao's extension of it directly uses the difference between the compressional and shear arrival times, and both require velocity models for the entire region between the source and receiver. On the other hand, the method presented here allows the imaging of the surface of the salt by using only the velocities in the limited region between the interface (in the case of salt imaging, the salt face), together with the polarization of the direct compressional and a measured time delay between compressional and shear arrivals.

Interferometry uses crosscorrelation and summation of data recorded at different receiver locations to approximate a data set that would have been acquired with a source located at each of the receiver locations and recorded by the other receivers. Interferometry can be considered to be a redatuming process in which new seismic responses corresponding to "virtual sources or receivers" are constructed by cross-correlating seismic observations recorded at different locations (Schuster, 2001; Curtis et al., 2006).

Interferometry has been applied to the VSP geometry by, e.g., Hornby et al. (2005, 2006), Xiao et al. (2006), Zhao et al. (2006), Roberts et al. (2009), and Yu and Hornby (2009). In the application to VSP data, the interferometric method takes advantage of the fact that for an offset source and receivers in a vertical well close to a steep-dip structure, the receivers record the wavefield on its way toward the steep structure, and then the reflected wavefield after it has been scattered back from the steep structure. As the incoming field is correlated with the backscattered field, the crosscorrelation between the two will have a peak at a time corresponding to twice the distance from the receiver array to the steep structure. The distance d to the structure could be found from an equation very similar to equation 1:

$$d = \frac{\Delta t^{ir}}{\frac{1}{v_r} + \frac{1}{v_i}}, \tag{11}$$

where Δt^{ir} is the time delay between the incoming and the backscattered wavefields and v_i and v_r are the propagation velocity for the incoming and reflected fields, respectively. Critically, however, whereas the denominator in equation 1 is the difference between the two slownesses, the denominator in equation 11 is the sum of the same two slownesses. This is related to the fact that the two wavefields used with equation 1 both move generally in the same

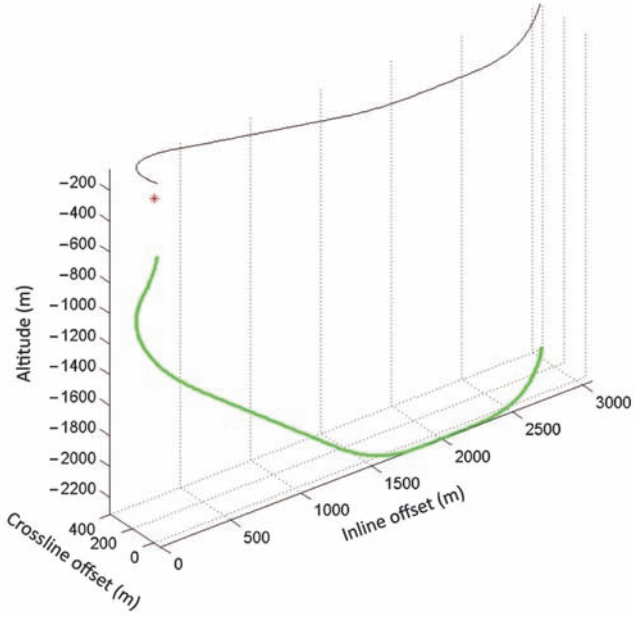

Figure 3. The trajectory of Oseberg B-24 after rotating the coordinate system in the horizontal plane around the wellhead at location (0,0,0) to minimize the excursion transverse to the well. The green dots mark the section of the well over which the VSP data were acquired. The black trace is the projection of the well onto the horizontal plane.

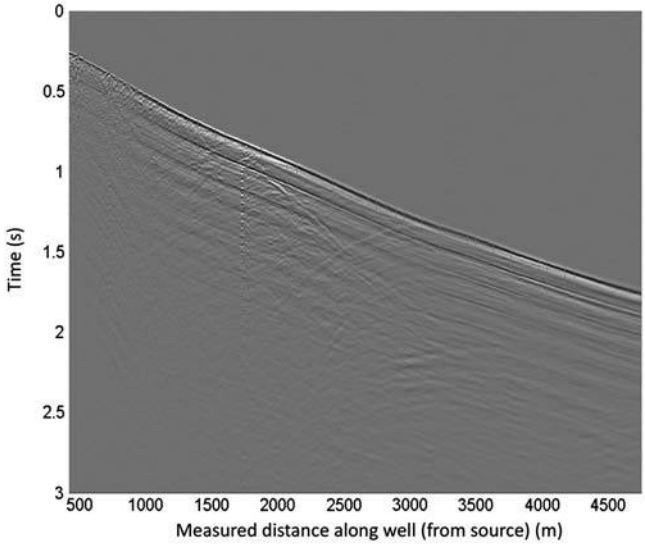

Figure 4. Inline horizontal components of data acquired in the mostly horizontal well.

direction, whereas the wavefields used with equation 11 move in opposite direction.

APPLICATION TO DATA

Oseberg B-24, as sketched as a cartoon in Figure 1, is an extended-reach well with a total length of around 4500 m. From a length of around 3000 m, the well is essentially horizontal at a maximum depth of around 2200 m and at the end reaches an offset of around 3000 m from the well head.

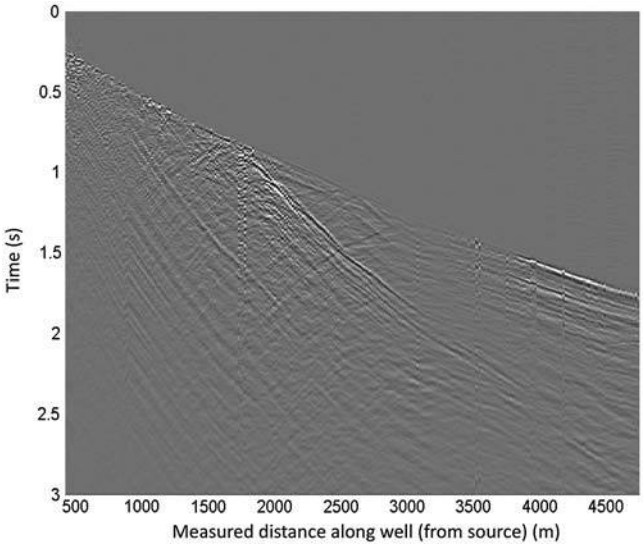

Figure 5. Crossline horizontal components of data acquired in the mostly horizontal well.

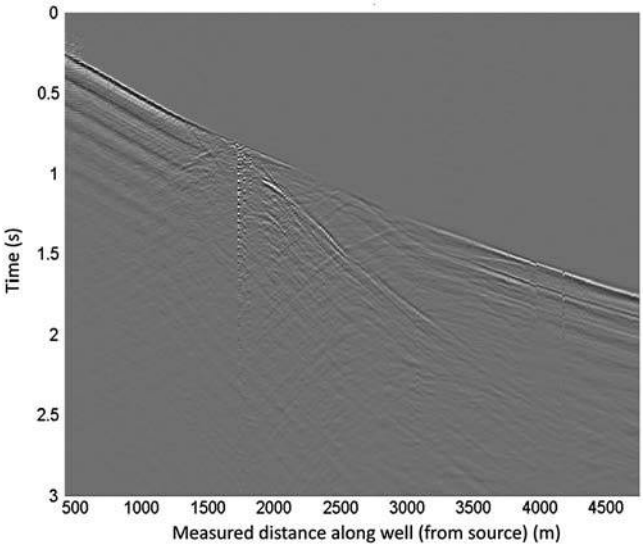

Figure 6. Vertical components of raw data acquired in the mostly horizontal well.

The VSP data were acquired using a four-level Schlumberger versatile seismic imager tool equipped with 3C fixed-axis geophone accelerometers. The wireline tool was pulled down through the maximum depth of the well by a borehole tractor. Data were recorded using a sample interval of 2 ms, and a depth interval of 15.25 m, starting at a depth of 4800 m in a 7-in (17.8-cm) liner, and stopping at 484 m, into triple 30-in (76-cm) casing.

For the data set used in this study, the source, deployed at the rig, consisted of 3×150 in^3 Sercel G. Gun air guns (for a total of 450 in^3, or 7.37 dm^3). The source was fired at least five times

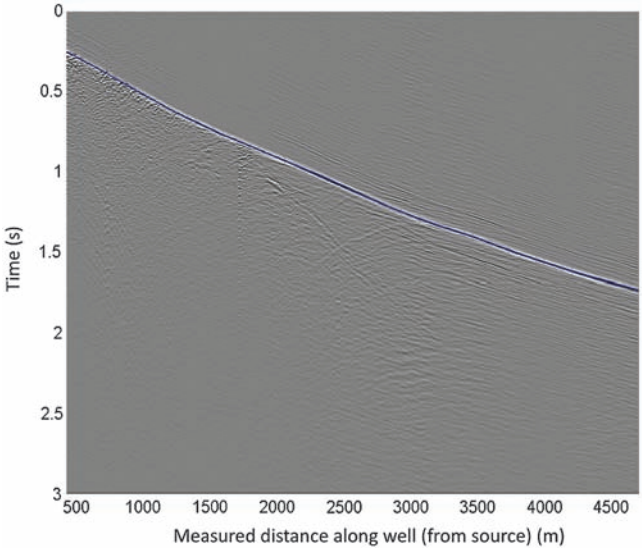

Figure 7. Horizontal components of data acquired in the mostly horizontal well. The blue line marks the time of arrivals for the direct compressional waves. The data have been deconvolved using an estimate of the direct compressional wave.

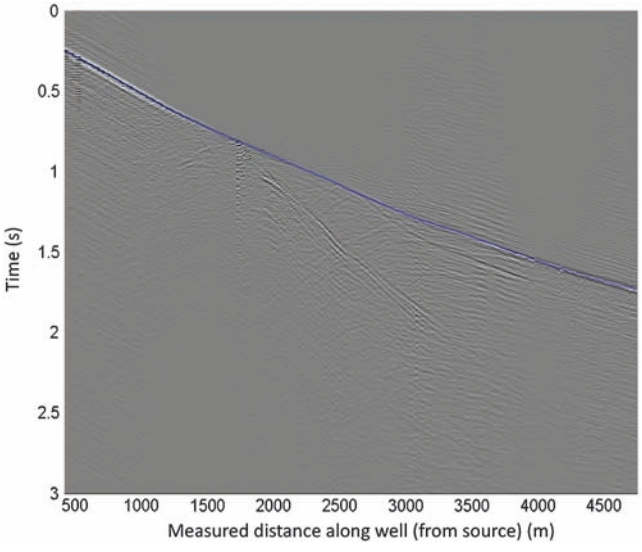

Figure 8. Vertical components of data acquired in the mostly horizontal well. The blue line marks the time of arrivals for the direct compressional waves. The data have been deconvolved using an estimate of the direct compressional wave.

per tool setting, under the control of the Schlumberger TrisorOFS digital gun controller.

Figure 3 shows the well in 3D space after rotating the coordinate system in the horizontal plane. The rotation was centered at the wellhead, for convenience chosen as the center of origin for the reference system. The rotation was performed to have the well and the data referenced to a system in which the well is mostly confined to the (x, z)-plane, i.e., the plane that minimizes the well excursion in the y-direction. After the rotation, the data were treated as if they essentially had been acquired in a 2D geometry.

Figures 4, 5, and 6 show the inline, crossline, and vertical rotated data. The horizontal axis gives the "measured depth," or the distance along the well below the Kelly bushing (KB). One may note the significant residual presence of shear energy on the crossline transverse components in Figure 5. This residual energy is primarily due to the 3D nature of the formation and partly due to the well not being, strictly speaking, confined to a plane. The residual transverse energy is dominated by mode conversions at "measured depths" of 700 and 1700 m. One may also notice that the direct compressional

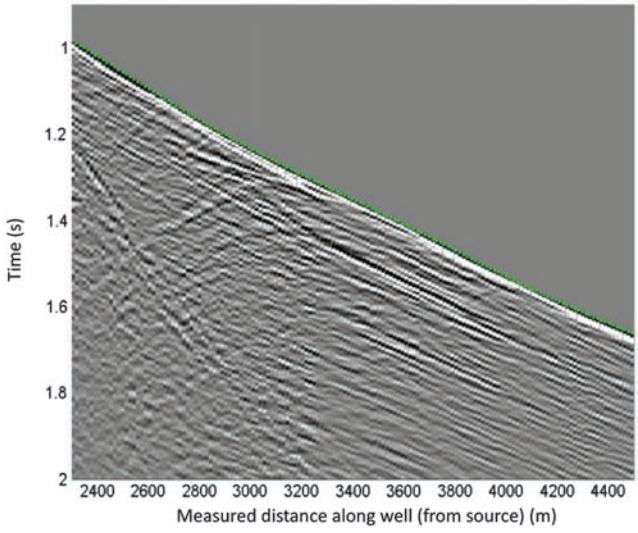

Figure 9. Details of data from Figure 7, horizontal components of data acquired in the mostly horizontal well, displayed as a function of distance along the wellbore. The dotted green line marks the time of arrivals for the direct compressional waves. The data have been deconvolved using an estimate of the direct compressional wave.

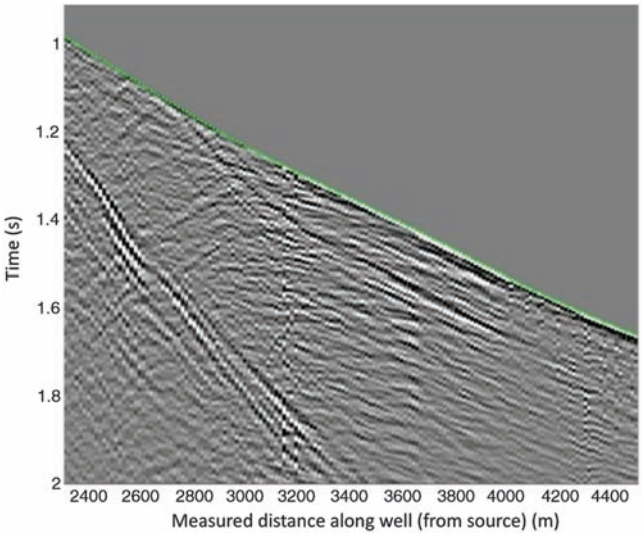

Figure 10. Details of data from Figure 8, vertical components of data acquired in the mostly horizontal well, displayed as a function of distance along the wellbore. The dotted green line marks the time of arrivals for the direct compressional waves. The data have been deconvolved using an estimate of the direct compressional wave.

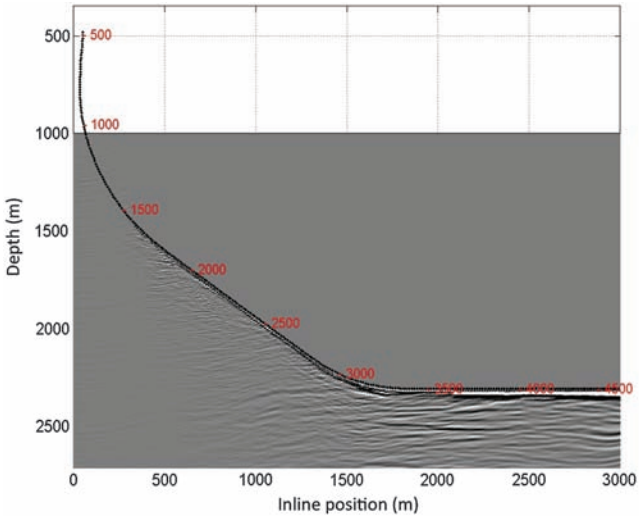

Figure 11. Image obtained from converted shear. The data have been migrated with a formation dip aperture of $\pm 15°$. Gently dipping features can be seen below the well. The measured depth (measured relative to the KB) is indicated along the well.

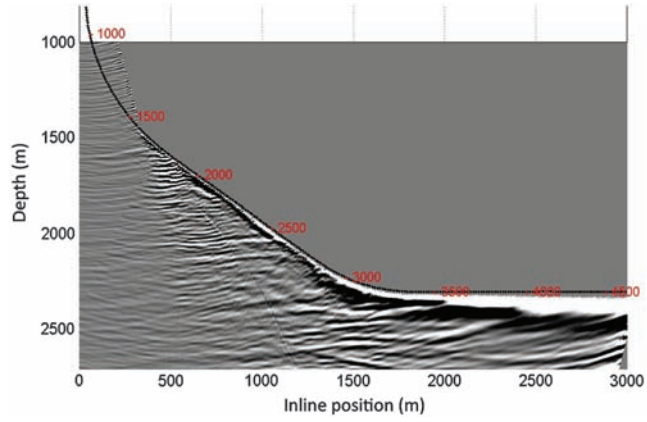

Figure 12. "Conventional" image obtained from reflected compressional waves. The data have been migrated with a formation dip aperture of $\pm 15°$. Gently dipping features can be seen below the well, as well as significant, steeper dipping features, artifacts related to converted shear not sufficiently attenuated by the migration process. The measured depth (measured relative to the KB) is indicated along the well.

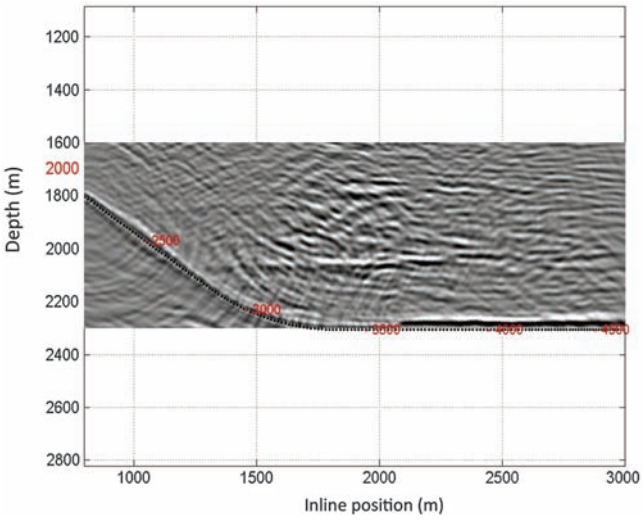

Figure 13. Image obtained from the downgoing shear waves in the vertical plane, containing shear converted between the source and receivers. At a depth of around 2050 m, an interface can be seen above the well at a distance of around 200 m.

arrivals in the vertical components in Figure 6 show a change of sign in the deepest (horizontal) part of the well relative to the shallowest (vertical) part of the well, indicating that at the furthest offsets, the direct compressional waves have turned and are propagating upward.

The data were deconvolved using the semblance-weighted deconvolution operator described by equation 10. The resulting compressed inline horizontal and vertical components are displayed in Figures 7 and 8. The light blue lines mark the arrival times for the direct compressional wave. Starting at an offset of around 1250 m and extending about 2 km beyond that, Figures 9 and 10 show close-up views of the deconvolved horizontal and vertical components of data over a depth range of about 2 km.

Figure 11 shows the reflection image obtained from converted shear. The measured depth is indicated along the well trajectory. Figure 12 shows the compressional reflection image. For both images, we used a formation-dip aperture of $\pm 15°$. The total unseparated, deconvolved wavefield is submitted to the migration, and the separation is done entirely within the migration operation (according to equation 6).

The two images — the reflection and the backscattered conversion image — show essentially the same gently dipping structures

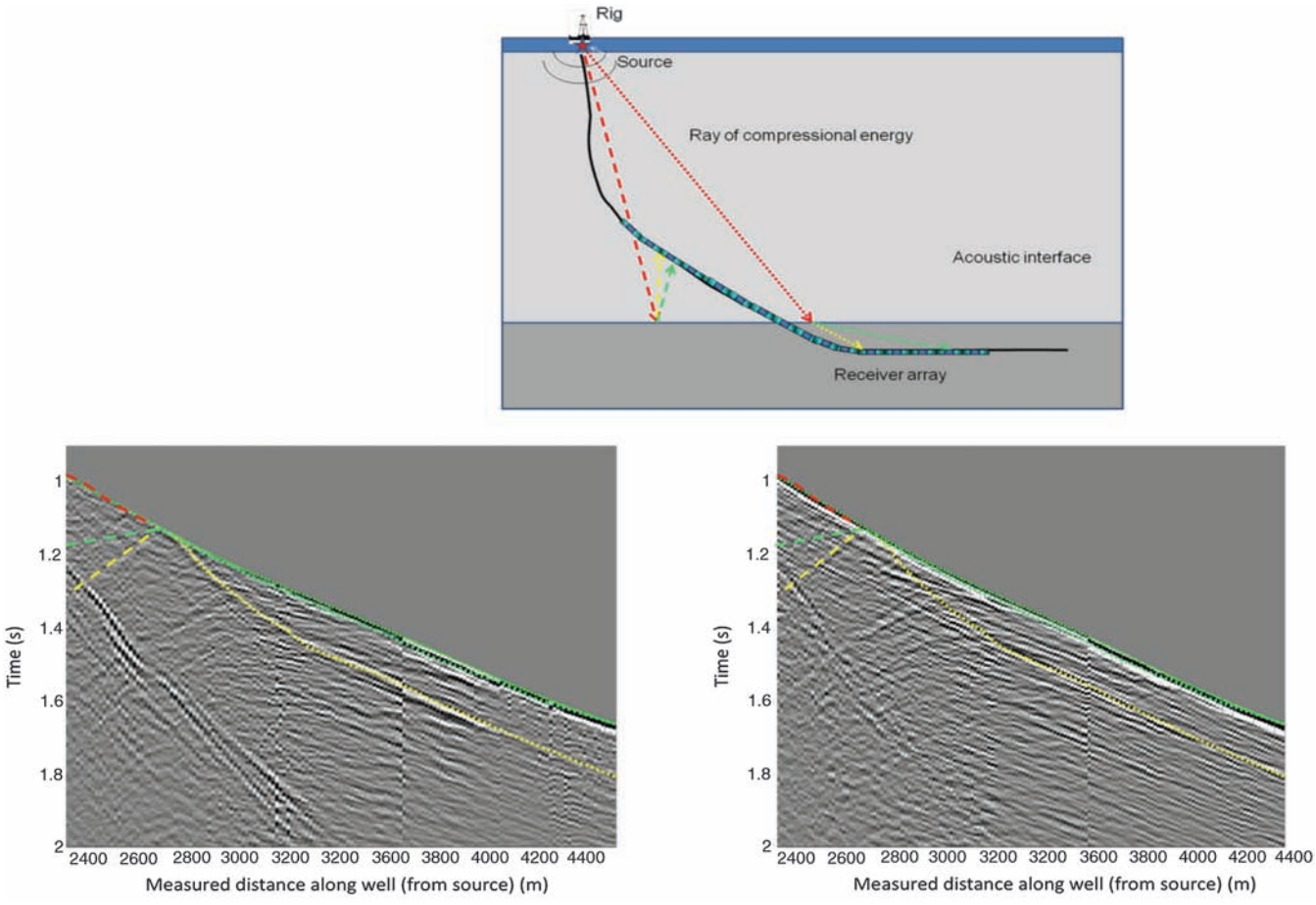

Figure 14. The deconvolved data from Figures 9 and 10 with the most prominent components that contribute to the reflection images (dashed green for upgoing compressional and dashed yellow for the upgoing shear in the vertical plane) and to the transmission image (dotted yellow for the corresponding, downgoing shear).

and interfaces below the well. At the larger measured depths (more than 3000 m below KB), the compressional image becomes largely low-frequency, dominated by the large-angle scattering. In addition, in the shallower part of the well, the compressional reflection image shows significant, steeper dipping features close to the wellbore. These features are most likely artifacts related to converted shear not sufficiently attenuated by the wavefield separation built into the migration process. This could also partly be caused by the shear and compressional wavefields, when converted or transmitted through an interface, are not mutually perpendicular. In general, and as should be expected because of the shorter wavelength of the shear waves, the converted-shear reflection image shows better resolution than the compressional image. In particular, one gets a better image of the reflector approached by the well near the heel of the well at around a vertical depth of 2250 m (measured depth of around 3150 m). It is not clear from the image whether this reflector is intersected by the well. There is some evidence of an additional interface coming really close to the well at a measured depth of around 4000 m.

The feature seen on both images to intersect the well at a measured depth of about 2650 m (vertical depth 2050 m and horizontal offset 1250 m from the well head) is of special interest, and will be discussed next. From the display of deconvolved data in Figures 9 and 10, we see evidence of the well penetrating an interface at a measured depth of 2650 m. This interface appears to be generating reflected compressional waves, as well as significant amounts of converted shear, in a reflected and a transmitted mode. The converted transmitted shear is particularly visible on the vertical components, which is what should be expected for the large source-receiver offsets encountered this deep into the well. The event starts as an obvious slow shear event near the point where the well penetrates the interface, but then deeper into the well, the wave appears to attain the same velocity as the direct compressional wave.

This somewhat unusual behavior is what generated the idea of converted-shear transmission imaging, which is the subject of this paper. The only way we could make apparent sense of the observations was by considering that we were not looking at fixed-point scattering, but rather a mode conversion point moving along an interface roughly parallel to the well. After the deconvolution based on the direct compressional energy, in accordance with the discussion in the previous section, the delay between the arrival at the wellbore of the direct compressional and the converted waves is a measure of the distance from the well. This means that the mode conversion takes place along an interface that is mostly parallel to the wellbore.

It should also be noted that because the apparent velocity of this shear event is the same as for the primary, compressional event, it would be a problem trying to separate the compressional and shear

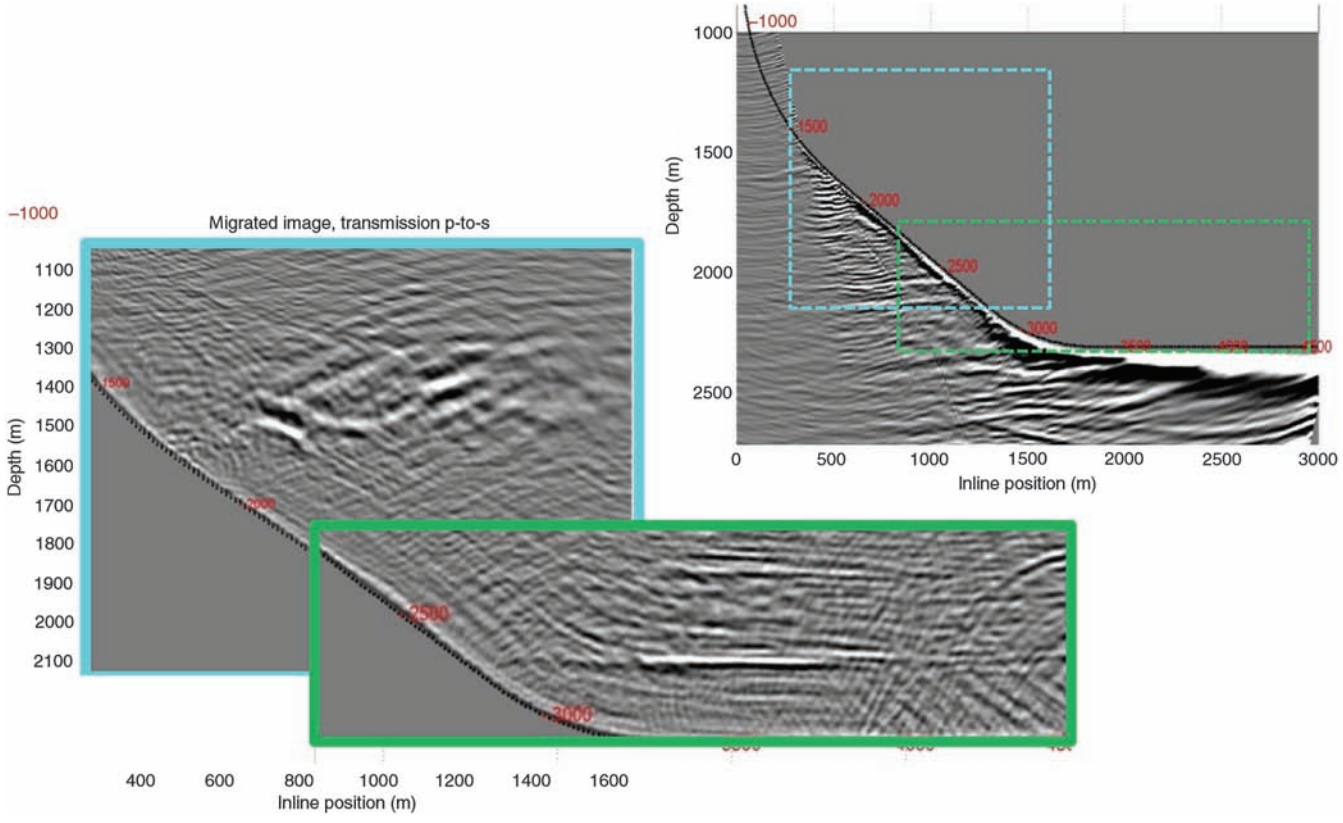

Figure 15. On the top right, details of the image obtained from the upgoing compressional wavefield (from Figure 12). The data have been migrated using a formation-dip aperture of ±15°. Below this and on the left, superimposed one on the other, are two images generated from downgoing converted shear. The dotted outlines on the "conventional" image represent the aperture of the images obtained from the converted shear. At a vertical depth of around 2100 m, an interface can be seen above the well at a distance of around 200 m. At a vertical depth of about 1500 m, several distinct objects can be seen. These are interpreted as cemented Oligocene sand bodies.

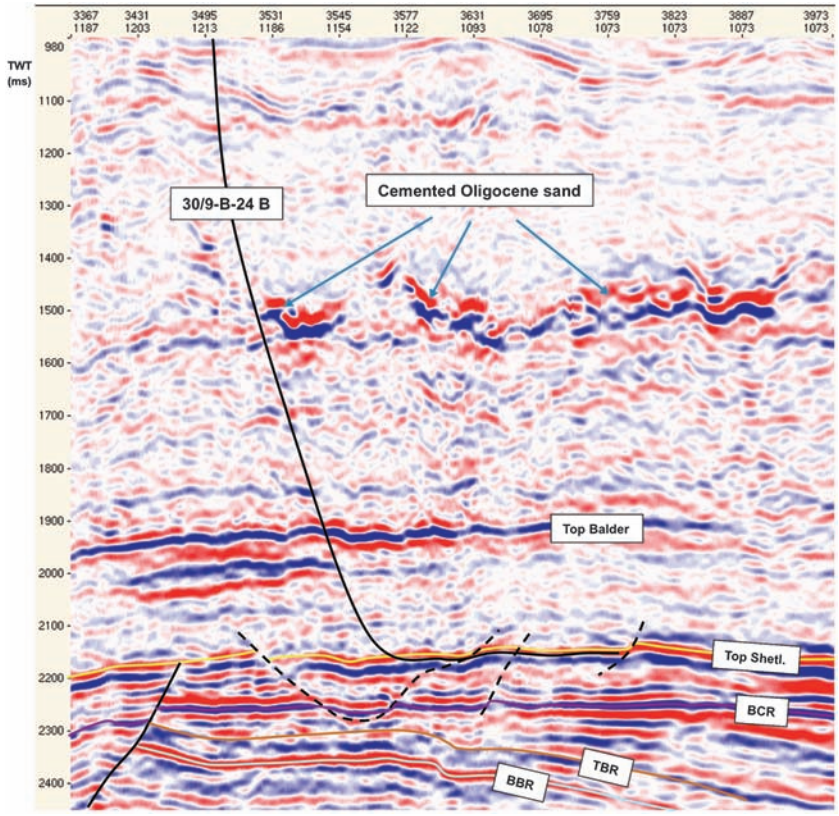

Figure 16. Window of interpreted marine surface-seismic data along Oseberg B-24 with the well plotted in offset versus equivalent seismic two-way time. The events labeled "Top Balder" and "Cemented Oligocene sand" are imaged by VSP data using the transmitted, converted shear.

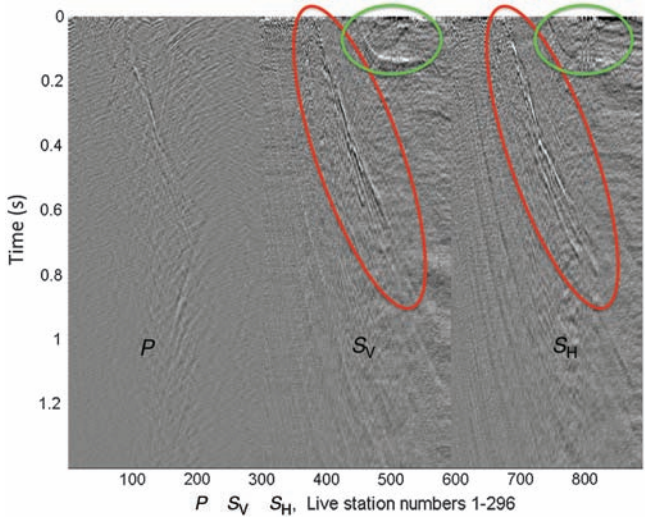

Figure 17. The deconvolved data, after separation into compressional and vertical and horizontal shear. The time (vertical axis) is relative to the compressional, direct arrivals. From the left are shown 296 compressional components, followed by 296 vertical shear, and finally 296 horizontal (transverse) shear components. The data are normalized individually by level, such that the relative scaling of the three components are preserved. The green ovals indicate the shear converted from the mostly horizontal feature above the well, the Top Balder. The red ovals indicate the shear energy converted at the shallower, Oligocene sand bodies.

components based on the difference in velocities. This problem is avoided by doing the wavefield separation inside the migration kernel following the prescription that Haldorsen (2002) gives.

Figure 13 shows the image obtained by mapping the conversion points for shear waves converted between the source and the receivers, essentially using equation 5 and the projection process described by equation 7. Although, as we have pointed out in the Introduction, the direct compressional and the converted shear are not perpendicular to each other, the location should be correct, and with a cosine radiation pattern, the error in the amplitude should be of the order of the square of the error in angle (as measured in radians). At a vertical depth of around 2050 m, the image shows an interface located above the well at a distance of around 200 m, intersecting the well at a measured depth of around 2650 m, consistent with discussions above.

In Figure 14, we show the approximate traveltimes for the most prominent components that contribute to the reflection images and the transmission image and the deconvolved data from Figures 9 and 10 with the most prominent components that contribute to the reflection images from Figures 11 and 12, and the transmission image from Figure 13. We have used dashed green for upgoing compressional, dashed yellow for the upgoing shear polarized in the vertical plane, and dotted yellow for the downgoing shear polarized in the vertical plane. To help with identification, we have included a graphic color key in the top-panel schematics in the figure.

When the image aperture is opened to include a more shallow section of the formation, several distinct, strong anomalies appear at a vertical depth of around 1500 m. These anomalies, seen on the collation in Figure 15, are interpreted as cemented Oligocene sand bodies. These bodies also show in surface-seismic images. Figure 16 shows a window of marine surface-seismic data along the well with the well plotted on top in equivalent seismic two-way time (from Petersen et al., 2004). The Oligocene sand bodies generate the high-energy "streaks" seen diagonally across the data in Figures 5, 6, and 8. The event on the surface-seismic image labeled "Top Balder" is identified with the horizon intersected by the well at a measured depth of 2650 m, as discussed above. The path of the planned well plotted in seismic reflection times as a solid black curve on the top surface-seismic image. With no control over the processing and depth conversion of the surface-seismic data and with the associated uncertainty in comparable depths, we cannot make a detailed quantitative comparison between the VSP and surface-seismic images. However, the image from the surface seismic data in Figure 16 shows the same qualitative structures as those seen in the collation in Figure 15.

The location of these sand bodies will only be correct to the extent that the arrival times of the compressional waves scattered off these bodies can be approximated by the direct arrival times. Otherwise they will have to be imaged using conventional converted-shear migration and a complete compressional velocity model.

Figure 17 shows more details for the data directly following the compressional, direct arrivals. The figure shows the deconvolved data, after separation into compressional and vertical and horizontal shear. The time (vertical axis) is relative to the compressional, direct arrivals. The data are normalized individually by level, such that the relative scaling of the three components are preserved. The green ovals indicate the shear converted from the mostly horizontal feature above the well, the Top Balder, which is penetrated by the well at around MD = 2700 m. Deeper in the well, the shear converted from Top Balder is delayed by about 0.25 s relative to the direct compressional. The red ovals indicate the shear energy converted at the shallower, Oligocene sand bodies, coming closest to the well at around MD = 1700 m. The shear converted at the Oligocene sand bodies appears to be equally distributed between the S_V and S_H components, indicating that the structures have significant crossline dip components. In contrast, the shear converted at the Top Balder appears mostly on the S_V component, consistent with only a slight crossline dip.

CONCLUSIONS

We have demonstrated how data generated by an offset acoustic source and an array of 3C receivers deployed in a wellbore can be used to image acoustic interfaces between the source and the receivers. In its simplest form, the method uses the polarization and signature of the direct compressional wave to find the shear wave polarized in the vertical well, perpendicular to the direct compressional wave, and it extrapolates the deconvolved shear signal along the direction of propagation back to its point of conversion, using velocities known locally around the well.

The method generates an image of the structure or interface along which the conversion took place. For extended-reach horizontal wells, this offers a unique possibility for locating the well relative to a shallower interface of changing acoustic impedance.

ACKNOWLEDGMENTS

The authors thank Statoil and Schlumberger for the authorization to present this work.

REFERENCES

Bostock, M. G., S. Rondenay, and J. Shragge, 2001, Multiparameter two-dimensional inversion of scattered teleseismic body waves, 1: Theory for oblique incidence: Journal of Geophysical Research, **106**, 30771–30782, doi: 10.1029/2001JB000330.

Cao, Z., and S. Greenhalgh, 1994, Finite-difference solution of the eikonal equation using an efficient, first-arrival, wave-front tracking scheme: Geophysics, **59**, 632–643, doi: 10.1190/1.1443623.

Chen, C.-W., D. E. Miller, H. A. Djikpesse, J. B. U. Haldorsen, and S. Rondenay, 2010, Array-conditioned deconvolution of multiple-component teleseismic recordings: Geophysical Journal International, **182**, 967–976, doi: 10.1111/(ISSN)1365-246X.

Curtis, A., P. Gerstoft, H. Sato, R. Snieder, and K. Wapenaar, 2006, Seismic interferometry — Turning noise into signal: The Leading Edge, **25**, 1082–1092, doi: 10.1190/1.2349814.

Haldorsen, J. B. U., 2002, Converted-shear and compressional images using projection imaging: 64th Annual International Conference and Exhibition, EAGE, Extended Abstracts, F031.

Haldorsen, J. B. U., D. E. Miller, and J. J. Walsh, 1994, Multichannel Wiener deconvolution of vertical seismic profiles: Geophysics, **59**, 1500–1511, doi: 10.1190/1.1443540.

Hornby, B., T. Fitzpatrick, F. Rollins, H. Sugianto, and C. Regone, 2005, 3D VSP used to image near complex salt structure in the deep water Gulf of Mexico: 67th Annual International Conference and Exhibition, EAGE, Extended Abstracts, E022.

Hornby, B., J. Yu, J. Sharp, A. Ray, and C. Regone, 2006, VSP: Beyond time-to-depth: 68th Annual International Conference and Exhibition, EAGE, Extended Abstracts, B031.

Leaney, W. S., and C. Esmersoy, 1989, Parametric decomposition of offset VSP wave fields: 59th Annual International Meeting, SEG, Expanded Abstracts, 26–29.

Michaud, G., D. Leslie, J. Drew, T. Endo, and K. Tezuka, 2004, Microseismic event localization and characterization in a limited aperture HFM experiment: 74th Annual International Meeting, SEG, Expanded Abstracts, 552–555.

Miller, D., M. Oristaglio, and G. Beylkin, 1987, A new slant on seismic imaging: Migration and integral geometry: Geophysics, **52**, 943–964, doi: 10.1190/1.1442364.

Petersen, S. A., M. E. Craven, S. Dingwall, S. Leaney, J-H. Meyer, and P. J. Smith, 2004, High resolution reservoir delineation by integrated seismic processing: A North Sea case study: 66th Annual International Conference and Exhibition, EAGE, Extended Abstracts, P214.

Roberts, M. A., B. E. Hornby, and F. Rollins, 2009, 3D salt-flank imaging with transmitted arrival VSP data: 79th Annual International Meeting, SEG, Expanded Abstracts, 4129–4134.

Rondenay, S., M. G. Bostock, and J. Shragge, 2001, Multiparameter two-dimensional inversion of scattered teleseismic body waves, 3: Application to the Cascadia 1993 data set: Journal of Geophysical Research, **106**, 30795–30807, doi: 10.1029/2000JB000039.

Schuster, G. T., 2001, Theory of daylight/interferometric imaging — Tutorial: 63rd Annual International Conference and Exhibition, EAGE, Extended Abstracts, A-32.

Sethian, J. A., 1996, Level set methods — Evolving interfaces in geometry, fluid mechanics, computer vision, and materials science: Cambridge University Press.

Shragge, J., M. G. Bostock, and S. Rondenay, 2001, Multiparameter two-dimensional inversion of scattered teleseismic body waves, 2: Numerical examples: Journal of Geophysical Research, **106**, 30783–30794, doi: 10.1029/2001JB000326.

Xiao, X., M. Zhou, and G. T. Schuster, 2006, Salt-flank delineation by interferometric imaging of transmitted P- to S-waves: Geophysics, **71**, no. 4, SI197–SI207, doi: 10.1190/1.2209550.

Yu, J., and B. Hornby, 2009, Comparison of interferometry and reverse time migration as approaches for VSP imaging of steep-dip boundaries: 79th Annual International Meeting, SEG, Expanded Abstracts, 4225–4226.

Zhao, X., Y. Li, and F. Doherty, 2006, Imaging of steep salt face and surrounding sediments using vertical seismic profile (VSP) converted waves: 76th Annual International Meeting, SEG, Expanded Abstracts, 2956–2960.